INTERNATIONAL JOURNAL FOR NUMERICAL METHODS IN FLUIDS
Int. J. Numer. Meth. Fluids 2010; **62**:1381–1410
Published online 21 May 2009 in Wiley InterScience (www.interscience.wiley.com). DOI: 10.1002/fld.2072

Quantification of phase shift in the simulation of shallow water waves

V. Sriram[1], S. A. Sannasiraj[1,*,†], V. Sundar[1], A. Schlenkhoff[2] and T. Schlurmann[3]

[1]*Department of Ocean Engineering, Indian Institute of Technology Madras, Chennai, India*
[2]*IGAW, University of Wuppertal, Wuppertal, Germany*
[3]*Franzius Institute, University of Hannover, Hannover, Germany*

SUMMARY

Numerical simulation of nonlinear waves to reproduce the laboratory measurements has been a topic of great interest in the recent past. The results reported in the literature are mainly focused on qualitative comparison or on the relative errors between the numerical simulation and measurements in laboratory and hence lack in revealing the existence of phase shift in nonlinear wave simulation. In this paper, the simulation of nonlinear waves in mixed Eulerian and Lagrangian framework using finite element method (FEM) is investigated by applying two different velocity calculation methods viz, cubic spline and least squares (LS). The simulated wave surface elevation has been compared with the experimental measurements. The coherence analysis has been carried out using the wavelet transformation, which gives a better understanding between the numerical and the experimental results with respect to the time–frequency space, compared with the conventional Fourier transformation. It is observed that the application of cubic spline approach leads to a higher phase difference for steeper waves. The present study has shown that the phase difference exists at the higher modes rather than at the primary period. For waves with steepness (wave height/wave length) higher than 0.04, LS approach is found to be effective in capturing the higher-order frequency components in the event of nonlinearity. In addition, the comparison of numerical simulations with that from PIV measurements for the tests with solitary waves is also reported. Copyright © 2009 John Wiley & Sons, Ltd.

Received 25 January 2009; Revised 26 March 2009; Accepted 27 March 2009

KEY WORDS: FEM; cubic spline; least squares; wavelet transform; PIV measurements; regular wave; cnoidal wave; solitary wave; phase difference

*Correspondence to: S. A. Sannasiraj, Department of Ocean Engineering, Indian Institute of Technology Madras, Chennai, India.
†E-mail: sasraj@iitm.ac.in

Contract/grant sponsor: DAAD (German Academic Exchange Service) short term fellowship

1. INTRODUCTION

The simulation of nonlinear waves using numerical wave tanks has been a problem under rigorous testing by researchers' world wide over the past few decades in order to reproduce the physical phenomenon of ocean waves as close as possible. The usual procedure to validate the simulated nonlinear waves has been by a qualitative comparison of the time histories with respect to the laboratory generated waves. The numerical simulation of nonlinear waves can be carried out by the conventional methods based on finite element method (FEM) and boundary element method (BEM) using mixed Eulerian and Lagrangian (MEL) approach proposed by Longuet-Higgins and Cokelet [1]. In this paper, FEM has been used. The above method has been successfully used by several researchers in the past [2–4] for the simulation of fully nonlinear waves. Most researchers adopted linear triangle element that lead to lower approximation for the velocity information, which still remain as a problem in the application of FEM. The use of iso-parametric elements [5] and six noded triangular elements [3] also reported the need for smoothing/regridding strategies. To overcome this shortcoming, the other methods of velocity estimation have been proposed namely global projection method, mapped finite difference (FD), least squares (LS) and cubic spline (CS). It has been found that both the LS approach and mapped FD produce identical results for a wide range of wave steepness [6], whereas, the global projection approach will lead to spurious velocity in the simulation results as reported by Sriram *et al.* [4] for structured mesh. Hence, in this paper, the results based on CS and LS approach are compared with the experimental measurements and the phase differences are reported. The qualitative comparison between the laboratory generation and numerical simulated waves has made by several investigators [2, 4, 6, 7], none of which revealed the phase difference quantitatively.

The comparison of the numerical simulation of breaking waves with that from physical measurements exhibits a slight deviation, which was claimed to be due to the dissipation of wave energy in the laboratory [8]. The phase difference can exist in numerical simulation due to two main reasons, one being the dissipation of the wave energy that results in the reduction of wave celerity and the other being due to the effect of surface tension that leads to an increase in the wave celerity in the laboratory generation of waves. A detailed note on this particular phase difference between the numerical and experimental measurements was attempted only for very small wave slope by Jensen and Grue [9]. The phase difference analysis has been carried out for the measurements of wave packets using Fourier analysis, and a difference of 0.01 ± 0.006 rad per wavelength was reported between the numerical and the physical measurements. Their numerical simulation was based on a linear code. Apart from this analysis, to the best of the knowledge of the author's, the comparison between the nonlinear wave simulation and the corresponding physical measurement has not been reported. The analysis can be carried out in the frequency domain and the Fourier analysis only give mean phase angle in the time series. However, the time–frequency evolution of the phase difference would give meaningful quantification. Schlurmann [10] described the time–frequency methods (namely wavelet transformation and Hilbert transformation) in hydrology and hydraulic engineering and Balaji *et al.* [11] applied time–frequency methods for the prediction of wave groups and breaking waves from a data buoy heave response time history. One of the most common tools for time–frequency space is the Wavelet analysis. By decomposing a time series into the time–frequency space, one can determine the frequency components in the signal as well as how these components evolve with time. The readers can refer Torrence and Compo [12] for details related to Wavelet analysis with reference to the practical implementation of the algorithms. It has been pointed out by Torrence and Compo [12] that

DOI: 10.1002/fld

in many studies, wavelet analysis has suffered from an apparent lack of quantitative results and highlighted the importance of statistical significance test. In order to examine the comparison between two (numerical and experimental) time series with large common power and to evaluate the phase relationship in time frequency space, cross wavelet transformation (XWT) is adopted, which is constructed from two continuous wavelet transform (CWT). Further, from wavelet coherence (WTC) between the two CWT, one can find significant coherence even if the common power is low. In this paper, the analyses are reported both qualitatively and quantitatively for numerical simulated (by adopting CS and LS approach) and laboratory generated wave elevation time series.

The following sections deal with a brief overview of the numerical simulation and the methods of velocity estimation, experimental setup, Wavelet analysis and the discussions for the regular and cnoidal waves. The results from the numerical model have been compared with particle image velocimetry (PIV) measurements of wave particle velocity in the laboratory and the spatial velocity comparisons for solitary wave are also reported in this paper.

2. FORMULATION AND NUMERICAL PROCEDURES

The nonlinear simulation of water waves has been carried out based on FEM using MEL approach. The two-dimensional fluid motion is defined with respect to the fixed Cartesian coordinate system, Oxz, with the z axis positive upwards from still water level. The water depth h is assumed to be a constant. The fluid is assumed to be incompressible and the flow as irrotational. Viscous forces have been neglected. This simplifies the flow problem that can be governed by Laplace's equation involving velocity potential $\Phi(x, z)$ given by,

$$\nabla^2\Phi = 0 \tag{1}$$

The schematic representation of the computational domain with the wave maker at one end and the prescribed Neumann and Dirichlet boundary conditions, on the three boundaries (bottom, left and right) as well as at the free surface are shown in Figure 1.

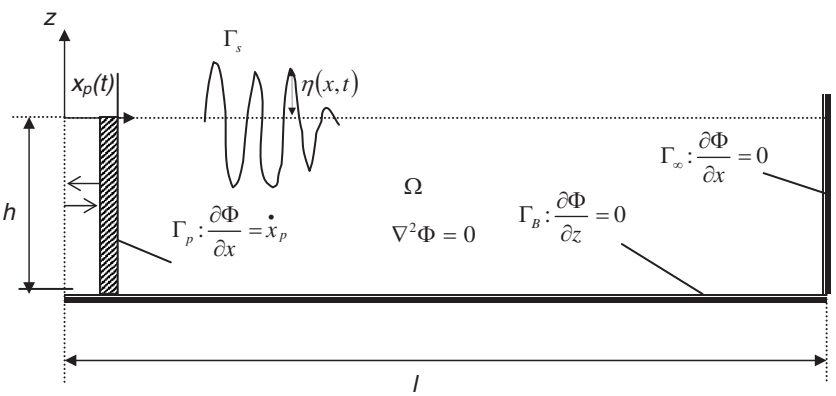

Figure 1. Computational domain with specified boundaries.

DOI: 10.1002/fld

Considering the flume bottom (Γ_B) as flat and no flow through it, the impermeable condition becomes

$$\frac{\partial \Phi}{\partial z} = 0 \quad \text{at } z = -h \text{ on } \Gamma_B \tag{2}$$

The far field is a fully reflecting (Γ_∞) wall at a distance 'l' from the wave paddle, leading to

$$\frac{\partial \Phi}{\partial x} = 0 \quad \text{at } x = l \text{ on } \Gamma_\infty \tag{3}$$

Motion of the wave paddle at the left end can be enforced by

$$\frac{\partial \Phi}{\partial x} = \dot{x}_p(t) \quad \text{at } x = x_p(t) \text{ on } \Gamma_p \tag{4}$$

where $x_p(t)$ is the time history of wave paddle motion. The nonlinear dynamic free-surface condition in the Lagrangian system is given by

$$\frac{\mathrm{d}x}{\mathrm{d}t} = \frac{\partial \Phi}{\partial x} \tag{5a}$$

$$\frac{\mathrm{d}z}{\mathrm{d}t} = \frac{\partial \Phi}{\partial z} - v(x)z \tag{5b}$$

$$\frac{\mathrm{d}\Phi}{\mathrm{d}t} = \frac{1}{2}\nabla\Phi\nabla\Phi - g\eta - v(x)\Phi \tag{5c}$$

where $v(x)$ is a damping coefficient defined as [13],

$$v(x) = \begin{cases} 0 & x < L - L_{\text{beach}} \\ \omega_{\text{beach}} \left(\dfrac{x - (L - L_{\text{beach}})}{L_{\text{beach}}} \right)^2 & L - L_{\text{beach}} \leqslant x \leqslant L \end{cases} \tag{6}$$

The frequency to be damped on the beach (ω_{beach}) is used to control the strength of the damping zone, while the parameter L_{beach} (beach length) is used to control the length of the damping zone.

The solution for the above boundary value problem is sought using FEM in this paper. In contrast with a linear boundary value problem, the water particle velocity at the free surface need to be evaluated in order to extract the free surface elevation at each time step. Once the velocity potential is obtained from FEM, the free surface horizontal and vertical velocities can be evaluated. However, the need for smoothing or regridding arises due to the inaccurate evaluation of the velocity from the velocity potential. Herein a brief review of the formulation and algorithm is provided.

Formulating the governing Laplace's equation constrained with the associated boundary conditions would lead to the following finite element system of equations [14]:

$$\int_\Omega \nabla N_i \sum_{j=1}^{m} \phi_j \nabla N_j \, \mathrm{d}\Omega|_{j,i \notin \Gamma_s} = -\int_{\Gamma_p} N_i \dot{x}_p(t) \, \mathrm{d}\Gamma - \int_\Omega \nabla N_i \sum_{j=1}^{m} \phi_j \nabla N_j \mathrm{d}\Omega|_{j \in \Gamma_s, i \notin \Gamma_s} \tag{7}$$

DOI: 10.1002/fld

where 'm' is the total number of nodes in the domain and the potential inside an element $\Phi(x,z)$ can be expressed in terms of its nodal potentials, ϕ_j, as

$$\Phi(x,z)=\sum_{j=1}^{n}\phi_j N_j(x,z) \tag{8}$$

Herein, N_j is the shape function and n is the number of nodes in an element. The above formulation does not have any singularity effect at the intersection point between the free surface and the boundaries, compared with other methods like BEM, boundary integral element method [14]. Linear triangular element is adopted. At the time of the initial simulation ($t=0$), the free surface elevation $\eta(x,0)$ and velocity potential, $\Phi(x,z,0)$ at the free surface are assumed to be zero for the wave generation problem.

At the subsequent time steps, for estimating the vertical velocity from the velocity potential, the backward FD method for unequal spacing of second order is used. The estimation of horizontal velocity is carried out based on CS approach proposed by Sriram *et al*. [4] and the LS approach by Turnbull *et al.* [15].

2.1. Velocity calculation methods

2.1.1. Least-squares approach. The LS approach to estimate the horizontal velocity is explained briefly as follows. Consider an arbitrary free surface node (i) connected to k neighboring nodes in the finite element mesh. Let $(X^k, \mathbf{Y}^k)$ denotes the position vector connected to the free surface node (i) to the nth ($n=1,\ldots,k$) node under consideration. Then, the velocities are estimated by using the following LS approximation in the matrix form as

$$\begin{pmatrix} \sum_{n=1}^{k} x,_l^n\, x,_l^n & \sum_{n=1}^{k} x,_l^n\, z,_l^n \\ \sum_{n=1}^{k} x,_l^n\, z,_l^n & \sum_{n=1}^{k} z,_l^n\, z,_l^n \end{pmatrix} \begin{Bmatrix} u \\ v \end{Bmatrix} = \begin{Bmatrix} \sum_{n=1}^{k} x,_l^n\, \phi,_l^n \\ \sum_{n=1}^{k} z,_l^n\, \phi,_l^n \end{Bmatrix} \tag{9a}$$

where

$$x,_l^n=\frac{(x_i-x_n)}{\sqrt{(x_i-x_n)^2+(z_i-z_n)^2}},\quad z,_l^n=\frac{(z_i-z_n)}{\sqrt{(x_i-x_n)^2+(z_i-z_n)^2}}$$

$$\phi,_l^n=\frac{(\phi_i-\phi_n)}{\sqrt{(x_i-x_n)^2+(z_i-z_n)^2}}$$

The above equation reduces to the following, if one knows the vertical velocity at ith node(v).

$$u_i=\frac{\sum_{n=1}^{k} x,_l^n\, \phi,_l^n-\sum_{n=1}^{k} x,_l^n\, z,_l^n v_i}{\sum_{n=1}^{k} x,_l^n\, x,_l^n} \tag{9b}$$

Similar procedure but without normalizing by the distance has been implemented in three-dimensional tanks also [2]. Ma and Yan [16] used a similar LS method to estimate the tangential velocities instead of u velocity and the normal derivative has been estimated using FD method.

DOI: 10.1002/fld

2.1.2. Cubic spline approach. In order to minimize the need for smoothing or regridding, splines are used as a velocity calculation method. Splines provide a better approximation of the behavior of functions that have abrupt local changes. Further, splines perform better than higher-order polynomial approximations. The efficient implementation of CSs as numerical differentiation for the evaluation of the tangential velocity in the simulation of waves using the lower-order BEM has been adopted by Sen *et al.* [17]. Sriram *et al.* [4] evaluated the horizontal velocity by fitting a CS to the 'x'-coordinates and $\phi(x,z)$ values. The end conditions are considered as the natural spline condition. To evaluate the smooth first derivative at the ith node, five nodes are considered (with two nodes on either side of the ith node) in order to minimize the effect of boundary constraints (natural spline condition).

Let us consider that f_i, f_i', f_i'', are continuous over a given interval. Based on the continuity condition, one can derive [18],

$$\frac{\delta x_i}{6} f''_{i-1} + \frac{\delta x_i + \delta x_{i+1}}{3} f''_i + \frac{\delta x_{i+1}}{6} f''_{i+1} = \frac{1}{\delta x_{i+1}}(f_{i+1} - f_i) - \frac{1}{\delta x_i}(f_i - f_{i-1})$$
$$i = 2, 3 \ldots k-1 \tag{10a}$$

The above equation leads to a set of $(k-2)$ linear equations for the k unknown functional values, f_i. The horizontal spacing (δx) between the two nodes is a known parameter. The above stated equation is solved by using the tridiagonal system of matrix assuming that the second derivatives at the ends are zero, i.e. the natural spline condition. In the present simulation, assuming $f_i = \phi_i$, the derivatives at a particular node are found out by considering two nodes on either side $(k=5)$, with the second derivatives $(\phi''_{i-2}, \phi''_{i+2})$ at the end nodes being set to zero. Following the evaluation of the second derivatives, the first derivatives can be estimated using Equation (10a) at the required node, which are derived in the intermediate steps of the CS interpolation

$$2f''_i + f''_{i+1} = \frac{6}{\delta x_i}\left(\frac{f_{i+1} - f_i}{\delta x_i} - f'_i\right) \tag{10b}$$

It should be noted that the above formula is valid only for calculating at the intermediate nodes and not at the inner boundary nodes. At the wave board, the velocity is assumed to be the input velocity and the velocity at the second node is evaluated by interpolation between the wave board and the third node (which will be known by the above method). Similarly, at the end of tank, the velocity is assumed to be zero.

A brief algorithm is given below. Assume the initial velocity potential and surface elevation. Digitize the entire domain using the required number of nodes and establish the element connectivity using a simple node generation formulae as in Wu and Eatock Taylor [14]. Apply FEM to obtain the velocity potential inside the fluid domain. The main part in the simulation is the velocity estimation. Recover the horizontal velocity using the suitable methodology on the free surface. Based on the velocities, update the free surface nodes using the dynamic and kinematic boundary condition based on Lagrangian/semi-Lagrangian form. The integration is carried out using the fourth-order Runge–Kutta method that requires repeated evaluation of velocity potential and velocity at the intermittent time steps to obtain the position at next time step. After the computation of the new

DOI: 10.1002/fld

free surface position and velocity potential, repeat the calculations as many times required until the termination time.

3. EXPERIMENTAL DETAILS

The experiments on the generation of regular and cnoidal waves were carried out in the wave flume at Franzius-Institute, University of Hannover, Germany. The flume is 100 m long, 2 m wide and 4 m deep. The water depth was adopted as 0.61 m in all the study. The existing system of water circulation to cool the wave paddle to avoid friction between the wave maker and the side walls was not working satisfactorily; thus, necessitating the usage of water through an external pipe leading to an increase in water level. An increase in the water level by about 2 cm in the flume was noticed and hence the measurement of water depth was carried out prior to every run. This plays a major role in the numerical simulation. Six numbers of wave probes were deployed in the wave flume at distances 4.849 m (WP1), 20.146 m (WP2), 25.136 m (WP3), 30.425 m (WP4), 40.406 m (WP5) and 50.609 m (WP6) from the wave paddle. The distances were measured using laser distometer. The input to the numerical model is from the feedback signal of the wave paddle in the flume. The input signal, water depth and the location of the measurement of time histories for a particular run are important parameters in the experiments that are essential for comparing the results with numerical simulation.

The generation of solitary waves was carried out in a glass flume, 24 m long, 0.3 m wide and 0.5 m deep at University of Wuppertal, Germany. A water depth of 0.2145 m for these studies was considered. This flume is equipped with a wave maker driven by a digital motor to which signals can be provided with high precision. The wave histories were recorded using Ultrasonic sensors at distances of 1.743 m and 6.74 m from the wave maker. The PIV measurements of water particle velocities were carried out at 3.45 m using the high-speed CCD camera having the resolution of 256×256 pixels. The camera is placed at 1.45 m (focus) from the center of the flume. The minimum focusing distance of the camera is 1 m. The field of view (FOV) is 0.26×0.26 m. The sampling interval for recording and for analysis was 0.002 s and 0.004 s, respectively.

4. WAVELET ANALYSIS

4.1. General

The analyses of the time series from numerical and experimental studies were carried out using the wavelet analysis. In this section, a brief overview about wavelet analysis, a suitable tool for the analysis of the transient, non-stationary or time-varying phenomena is provided. The theoretical background of wavelet analysis is described by Daubechies [19], whereas the details of wavelets are given by Weng and Lau [20] and Torrence and Compo [12]. In the context of Ocean Engineering, the wavelet transform has been successfully used to understand the dispersion of ocean waves [21], wave growth and breaking [22] and more recently for the identification of different types of ocean waves [11]. Wavelets are similar to, but, an extension of Fourier analysis and Computational wise, the wavelet transformation is similar to the fast fourier transformation and hence, it is an alternative to classical windowed fourier transformation. The major difference when compared

DOI: 10.1002/fld

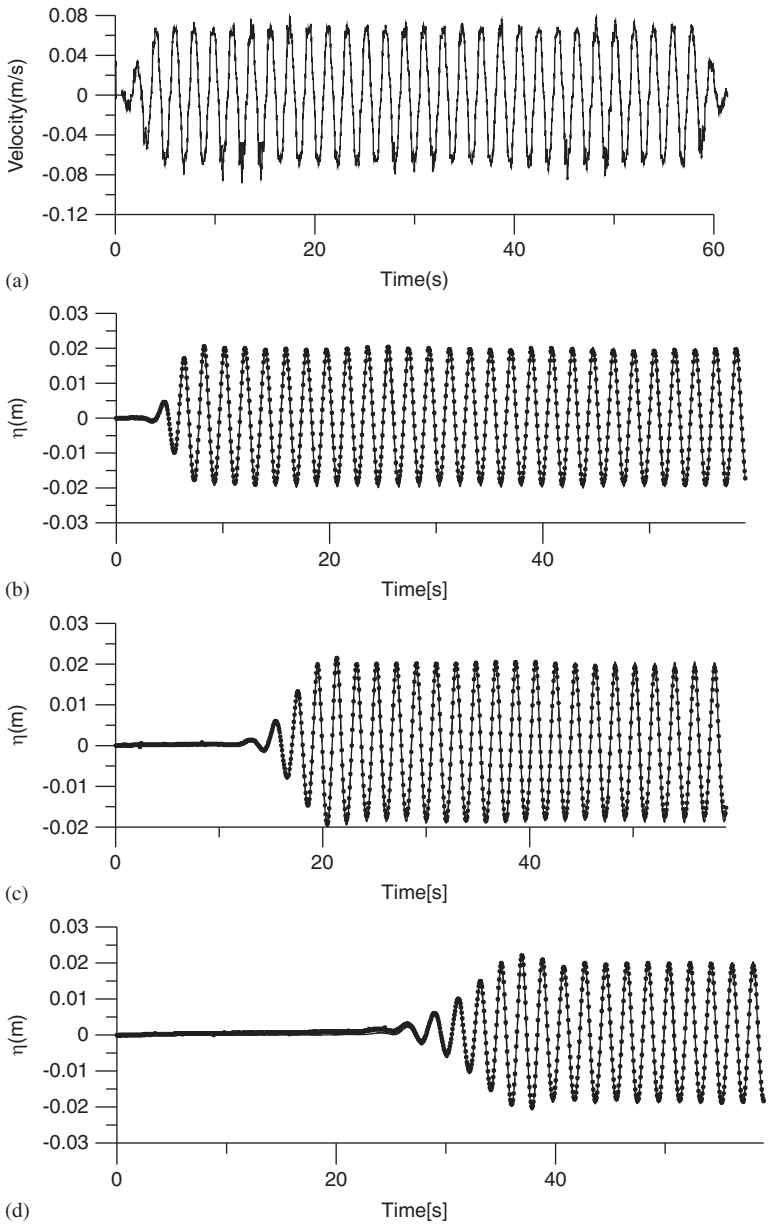

Figure 2. Regular wave (R1): (a) Input velocity; (b) time history at 4.849 m; (c) time history at 25.136 m; and (d) time history at 50.609 m.

DOI: 10.1002/fld

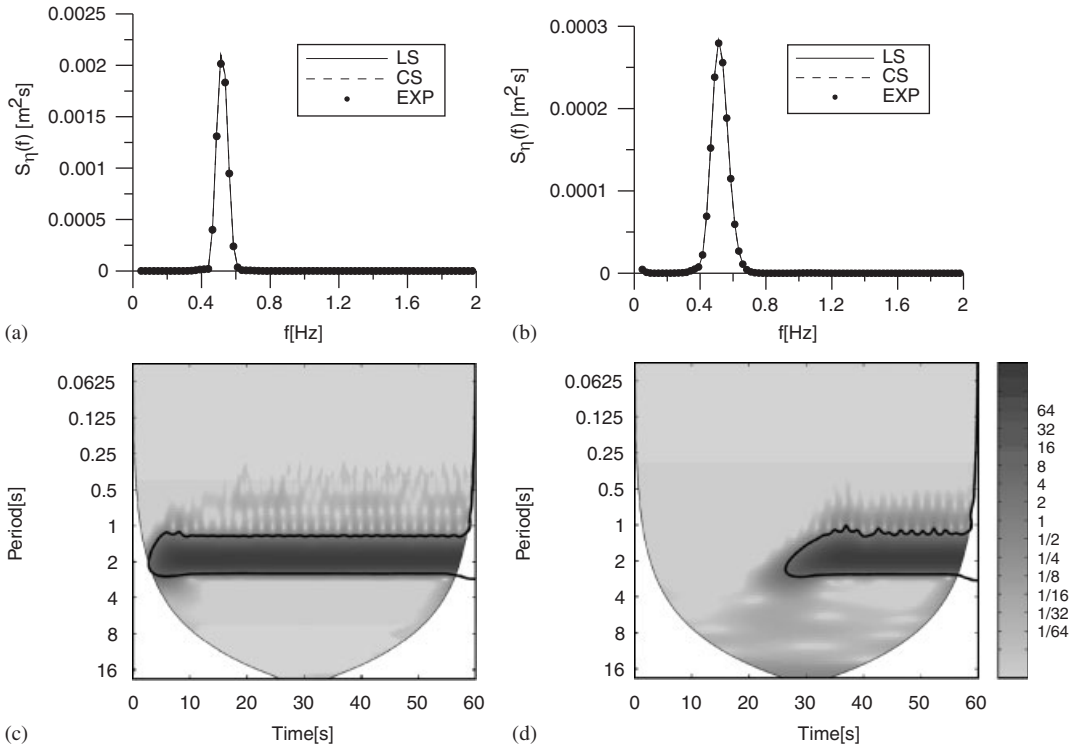

Figure 3. Fourier Spectrum at (a) 4.895 m (R1) and (b) 50.609 m (R1). Wavelet power for EXP at (c) 4.895 m (R1) and (d) 50.609 m (R1).

with the windowed fourier transformation is that the window in wavelet is already oscillating and is called mother wavelet, which is, in general, a non-harmonic functions.

4.2. Continuous wavelet transform (CWT)

In order to define a function $\psi(t)$ as mother wavelet, it must satisfy the following conditions:

(1) The function should be a zero mean process, so that it is inversible. This is known as the admissibility condition. Thus, the original signal can be obtained from the wavelet coefficients through the inverse transform.
(2) The function must have unitary energy, i.e.

$$\int_{-\infty}^{\infty} |\psi(t)|^2 \, \mathrm{d}t = 1 \tag{11}$$

This assures that the wavelet function has a compact support or has a fast amplitude decay enabling physical domain localization.

The Morlet wavelet, consisting of a plane wave modulated by Gaussian, is taken as the mother wavelet for the present study, which has been widely used by several researchers. It is proved to

DOI: 10.1002/fld

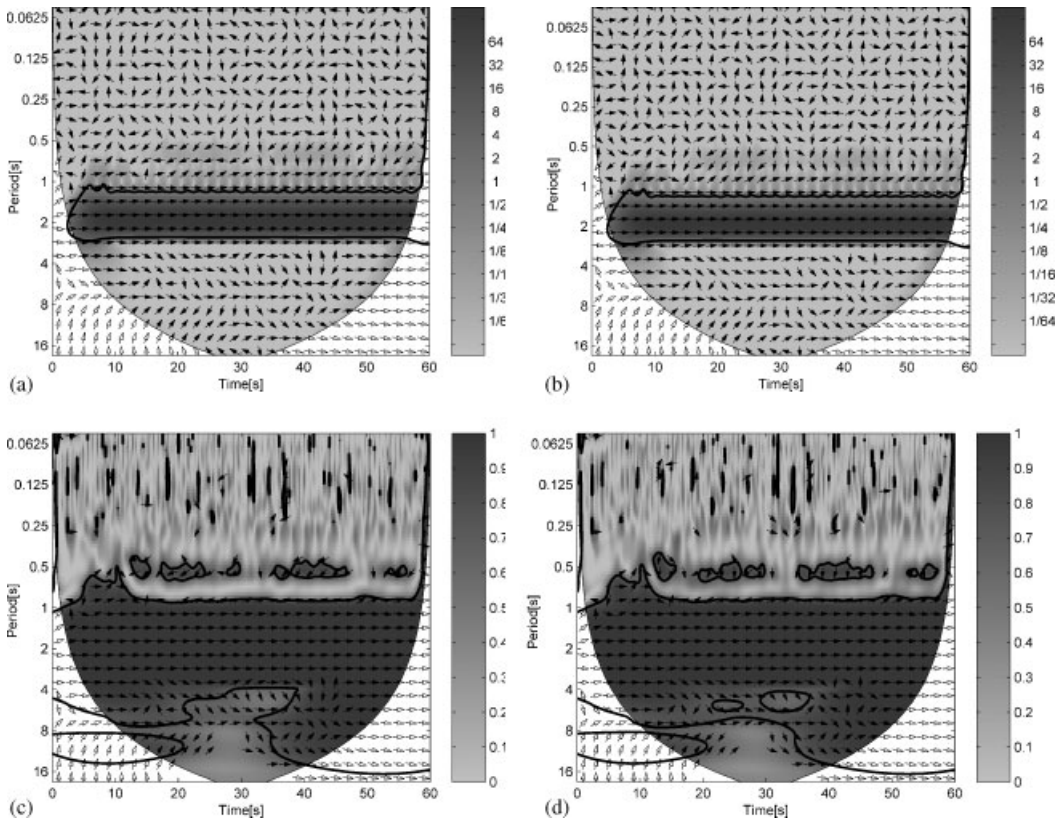

Figure 4. Cross Wavelet between (a) EXP-CS at 4.895 m (R1) and (b) EXP-LS at 4.895 m (R1). Wavelet Coherence between (c) EXP-CS at 4.895 m (R1) and (d) EXP-LS at 4.895 m (R1).

be efficient for its application to Ocean and Coastal Engineering problems due to its Gaussian nature [21, 22]. It is defined as

$$\psi(t) = \pi^{-1/4} e^{i\omega_0 t} e^{-t^2/2} \tag{12}$$

where ω_0 is the dimensionless frequency and is taken as 6 based on Farge [23] in order to satisfy admissibility condition.

The CWT [CWT, $W_x(a,t)$] of a one-dimensional signal $x(t)$ is given as

$$W_x(a,t) = \frac{1}{\sqrt{|a|}} \int_{-\infty}^{\infty} x(t) \cdot \psi^* \left(\frac{t-\tau}{a} \right) dt \tag{13}$$

in which ψ^* is the scaled and translated version of basis function. Herein, 'a' is the scaling factor and 'τ' is the translating or shifting factor and '$1/\sqrt{a}$' is the normalization factor to ensure that all wavelets have the same energy. The signal $x(t)$ is bounded in time so the wavelet transform is affected by edge effects, called as the cone of influence (COI) [12]. Statistical significance was also estimated against a red noise model as proposed by them.

DOI: 10.1002/fld

Table I. Wavelet phase angle for the test case $T=1.92\,\text{s}$, $H=0.04\,\text{m}$, $D=0.613\,\text{m}$ (R1).

Wavelet	WP 1 (deg.)	WP2 (deg.)	WP3 (deg.)	WP4 (deg.)	WP5 (deg.)	WP6 (deg.)
XWT1	0.49 ± 12.204	-2.24 ± 14.22	-2.74 ± 29.03	-1.42 ± 23.44	-1.22 ± 13.58	-4.38 ± 6.33
WTC1	-0.52 ± 20.6	-2.62 ± 22.42	-5.25 ± 35.60	-1.56 ± 22.03	-2.14 ± 37.51	-0.96 ± 23.05
XWT2	0.51 ± 12.26	-2.30 ± 13.95	-2.74 ± 28.99	-1.46 ± 23.37	-1.28 ± 13.52	-4.41 ± 6.32
WTC2	-0.51 ± 19.19	-2.55 ± 24.01	-5.68 ± 37.03	-1.55 ± 22.40	-1.85 ± 38.45	-1.41 ± 24.48

XWT1 and WTC1: EXPxCS, XWT2 and WTC2: EXPxLS, WP1 = 4.8495 m; WP2 = 20.146 m; WP3 = 25.136 m; WP4 = 30.425 m; WP5 = 40.406 m; and WP6 = 50.609 m.

4.3. Cross wavelet transform (XWT)

The analysis of the covariance of two time series (experimental and numerical) has been carried out using the cross wavelet transformation. The cross wavelet transform of the two time series $x(t)$ and $y(t)$ with wavelet transform, W_x and W_y is defined as

$$W_{xy}(a,t)=W_x(a,t)W_y^*(a,t) \tag{14}$$

where the asterisk denotes complex conjugate. The phase angle of W_{xy} describes the phase relationship between x and y, whereas the power is obtained from the magnitude of W_{xy} in the time–frequency space. In the present paper, the main interest is the phase difference between the components of the two time series, the mean and estimated confidence interval of the phase difference. The circular mean of a set of angles within the 5% statistical significant region (or 95% confidence) are estimated as in Zar [24], whereas, the confidence interval is difficult to interpret and hence, it is find out using the circular standard deviation [25].

4.4. Wavelet coherence (WTC)

This is an estimation of the intensity of the covariance of any two given time series in time–frequency space, unlike the XWT power, which is the estimation of common powers. Coherence (R) has been defined [26] as

$$R^2(a,t)=\frac{|S(s^{-1}W_{xy}(a,t))|^2}{S(s^{-1}|W_x(a,t)|^2)\cdot S(s^{-1}|W_y(a,t)|^2)} \tag{15}$$

where S is a smoothing operator, defined as, $S(W)=S_{\text{scale}}(S_{\text{time}}(W(a,t)))$. The scales in the time and frequency over which S is smoothening define the scales at which the coherence measures the covariance of the time histories considered. Torrence and Webster [26] reported the natural way to design the smoothing operator for the Morlet wavelet. The coherence significant levels was estimated using Monte Carlo methods with red noise to determine the 5% statistical significance level [25]. The circular mean as well as the confidence interval are calculated similar to XWT. The reason for the difference between the phase angles reported for the cross wavelet and coherence methods is because of the smoothing operator used in the coherence method.

DOI: 10.1002/fld

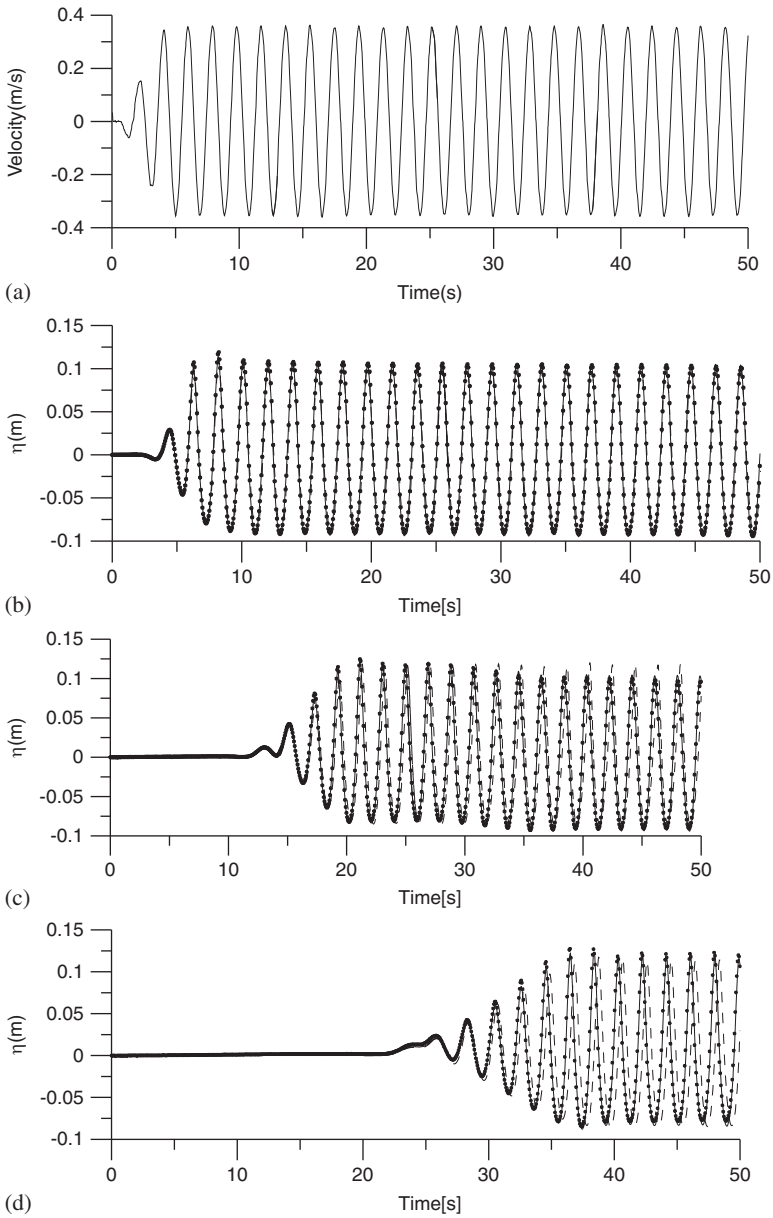

Figure 5. Regular wave (R2): (a) input velocity; (b) time history at 4.849 m; (c) time history at 25.136 m; and (d) time history at 50.609 m.

DOI: 10.1002/fld

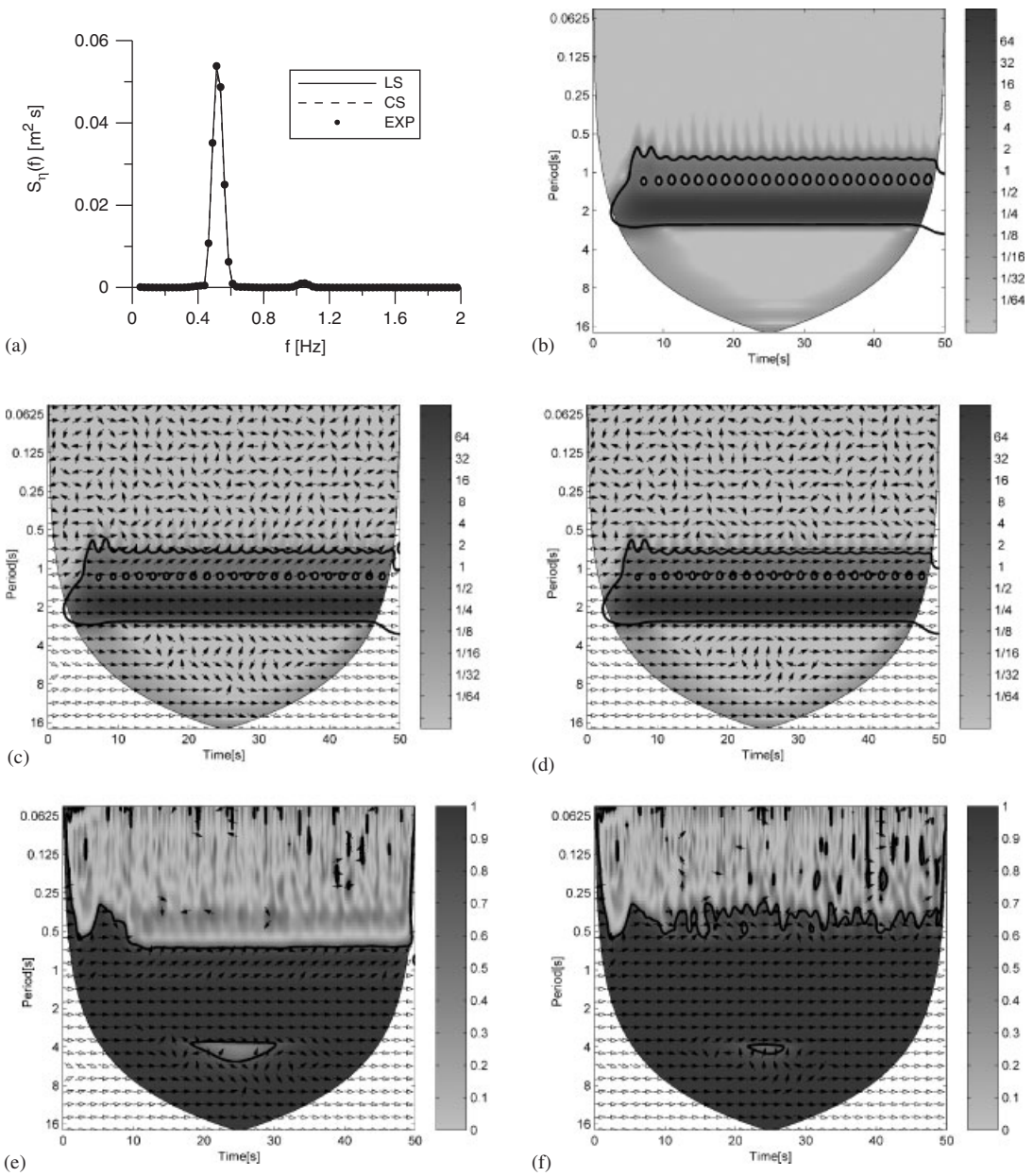

Figure 6. (a) Fourier Spectrum at 4.895 m (R2); (b) wavelet power for EXP at 4.895 m (R2). Cross wavelet between (c) EXP-CS at 4.895 m (R2) and (d) EXP-LS at 4.895 m (R2). Wavelet coherence between (e) EXP-CS at 4.895 m (R2) and (f) EXP-LS at 4.895 m (R2).

DOI: 10.1002/fld

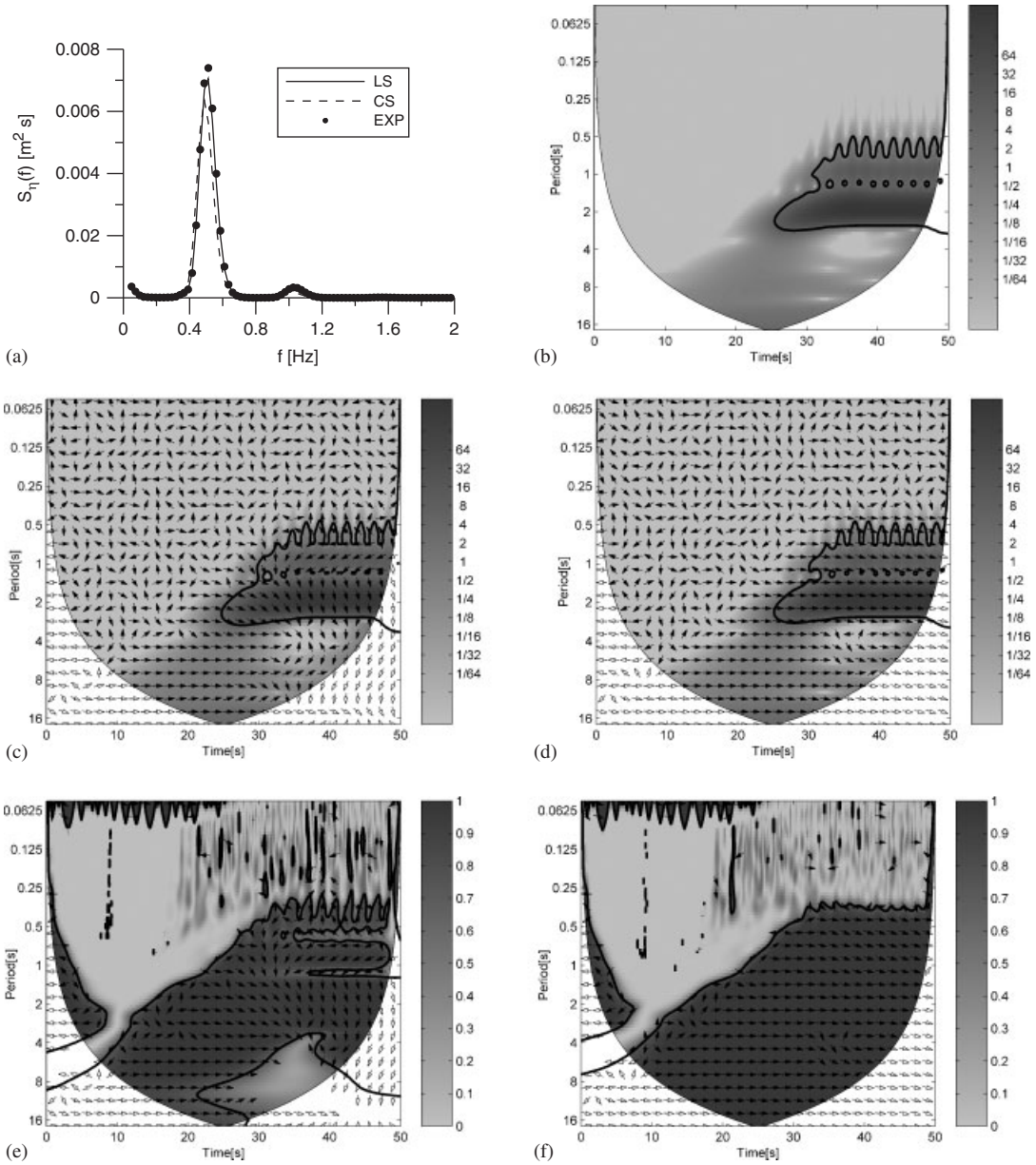

Figure 7. (a) Fourier spectrum at 50.609 m (R2); (b) wavelet power for EXP at 50.609 m (R2). Cross Wavelet between (c) EXP-CS at 50.609 m (R2) and (d) EXP-LS at 50.609 m (R2). Wavelet coherence between (e) EXP-CS at 50.609 m (R2) and (f) EXP-LS at 50.609 m (R2).

DOI: 10.1002/fld

Table II. Wavelet phase angle for the test case $T=1.92\,\text{s}$, $H=0.2\,\text{m}$, $D=0.621\,\text{m}$ (R2).

Wavelet	WP1 (deg.)	WP2 (deg.)	WP3 (deg.)	WP4 (deg.)	WP5 (deg.)	WP6 (deg.)
XWT1	−5.56±15.76	33.95±17.45	44.21±25.47	57.75±29.96	71.58±38.14	78.83±48.36
WTC1	1.93±26.65	12.25±34.69	28.10±40.92	28.45±49.20	31.18±66.86	36.52±73.99
XWT2	−4.79±2.678	−3.76±8.10	−1.50±5.21	3.32±7.00	8.91±4.760	9.74±5.51
WTC2	−2.11±24.05	−0.61±24.12	0.07±22.84	5.85±25.25	5.28±35.32	6.51±38.95

XWT1 and WTC1: EXPxCS, XWT2 and WTC2: EXPxLS, WP1 = 4.8495 m; WP2 = 20.146 m; WP3 = 25.136 m; WP4 = 30.425 m; WP5 = 40.406 m; and WP6 = 50.609 m.

Table III. Wavelet phase angle variation for different mesh sizes with a constant time steps ($T/100$) at: (a) WP3 (R2) and (b) WP6 (R2).

No. of nodes on the free surface per wave length	XWT for EXP-LS	WTC for EXP-LS	XWT for EXP-CS	WTC for EXP-CS
(a)				
30	2.27±8.45	2.85±24.06	47.09±27.02	29.64±41.88
40	−1.50±5.21	0.07±22.85	44.21±25.47	28.10±40.92
50	−2.56±2.80	−0.72±21.92	43.03±24.47	27.49±39.5
(b)				
30	24.54±13.01	16.52±44.51	84.16±76.43	37.191±51.86
40	9.74±5.51	6.51±38.95	78.83±48.36	36.52±73.99
50	4.85±3.20	3.19±25.90	77.136±47.17	35.81±73.09

Table IV. Wavelet Phase angle variation for different time step with a constant mesh sizes ($L/40$) at: (a) WP3 (R2) and (b) WP6 (R2).

Time step per wave period	XWT for EXP-LS	WTC for EXP-LS	XWT for EXP-CS	WTC for EXP-CS
(a)				
60	−1.08±5.24	0.20±26.00	44.90±24.90	29.76±44.50
100	−1.50±5.21	0.07±22.85	44.21±25.47	28.10±40.92
120	−1.99±5.36	−0.42±22.94	44.07±26.62	28.03±41.41
(b)				
60	12.40±6.56	7.19±45.32	82.21±47.58	40.80±82.56
100	9.74±5.51	6.51±38.95	78.83±48.36	36.52±73.99
120	9.80±5.60	5.73±39.67	78.28±52.55	32.28±75.04

5. RESULTS AND DISCUSSION

5.1. Regular waves

The experiments were carried out to generate a regular wave with a period of 1.92 s, and two diffeent wave heights, corresponding to wave steepness of 0.01 and 0.047. In numerical modeling, the number of nodes used in the horizontal and vertical directions is 1101 and 21, respectively. For

DOI: 10.1002/fld

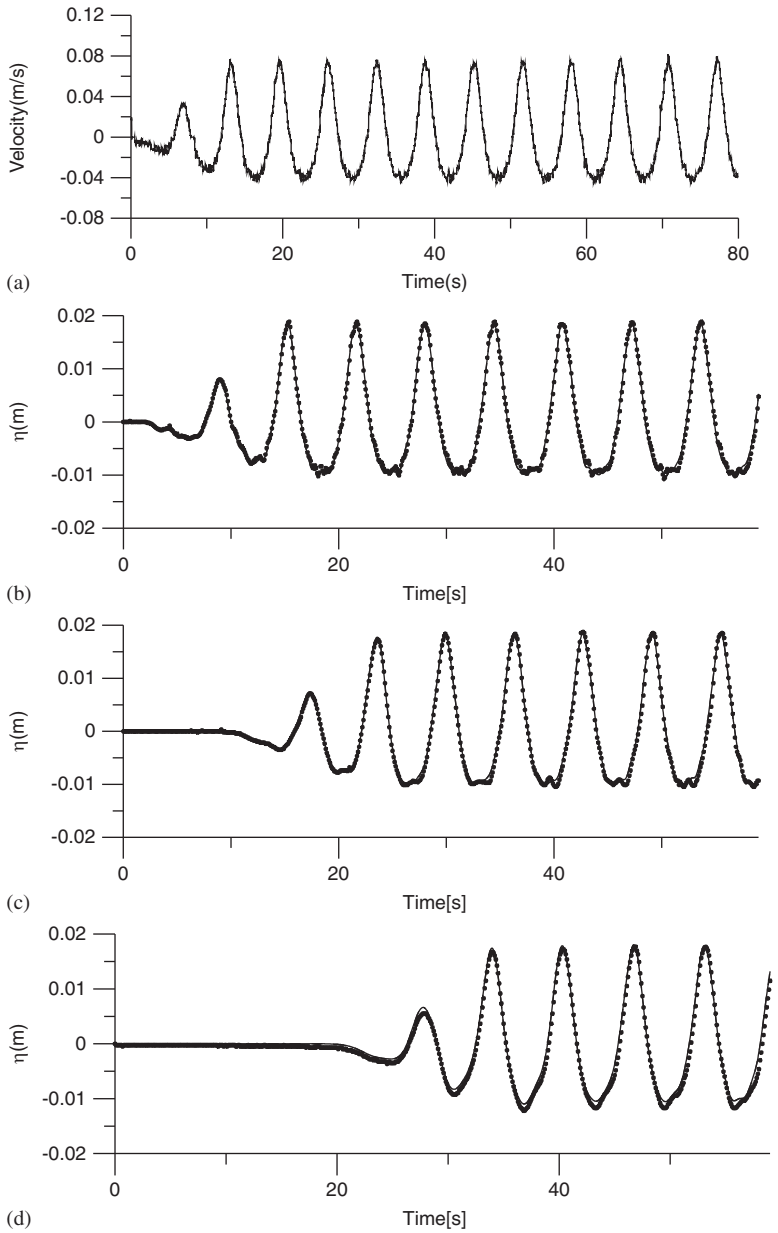

Figure 8. Cnoidal wave (CN1): (a) input velocity; (b) time history at 4.849 m; (c) time history at 25.136 m; and (d) time history at 50.609 m.

the case of CS approach, no regridding is applied, whereas, the regridding has been carried out for every 40 time steps while adopting the LS approach. The time step used for the calculations is 0.02 s. The numerical setup is kept constant for all the wave simulation reported in this paper, unless and otherwise quoted. The comparison of time histories from the experimental measurement

DOI: 10.1002/fld

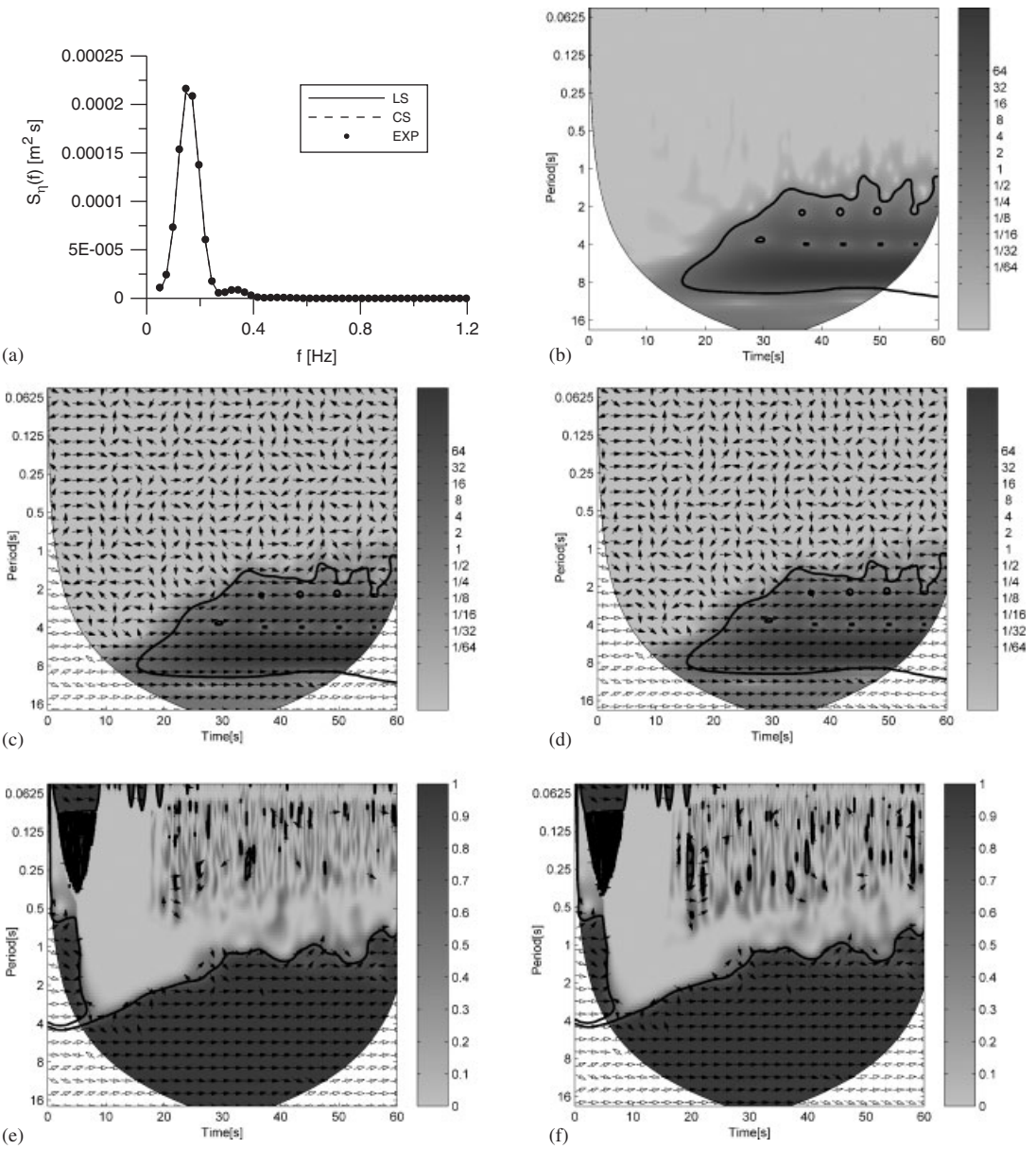

Figure 9. (a) Fourier spectrum at 50.609 m (CN1); (b) wavelet power for EXP at 50.609 m (CN1). Cross wavelet between (c) EXP-CS at 50.609 m (CN1) and (d) EXP-LS at 50.609 m (CN1). Wavelet coherence between (e) EXP-CS at 50.609 m (CN1) and (f) EXP-LS at 50.609 m (CN1).

and the numerical simulations at various locations along the length of the tank for waves with a steepness of 0.01 (wave height of 0.04 m) is shown in Figure 2. The input paddle velocity has been obtained by differentiating the measured paddle displacement, which resulted in spurious noises in the signal as can be seen in Figure 2(a). The wave surface elevation at a distance of 4.849, 25.136

DOI: 10.1002/fld

Table V. Wavelet phase angle for the test case $T=6.4$ s, $H=0.03$ m, $D=0.619$ m (CN1).

Wavelet	WP1 (deg.)	WP2 (deg.)	WP3 (deg.)	WP4 (deg.)	WP5 (deg.)	WP6 (deg.)
XWT1	-2.28 ± 1.571	2.18 ± 4.21	1.71 ± 6.057	3.59 ± 1.84	4.40 ± 2.4762	1.05 ± 2.15
WTC1	-1.82 ± 39.73	5.11 ± 34.09	0.00 ± 28.427	6.25 ± 34.61	-2.68 ± 39.10	3.01 ± 36.58
XWT2	-2.49 ± 1.470	0.62 ± 2.81	0.28 ± 4.9812	2.05 ± 1.56	2.44 ± 1.8406	-1.40 ± 1.94
WTC2	-1.36 ± 37.08	4.66 ± 35.38	-1.06 ± 29.00	5.36 ± 32.11	-3.91 ± 39.14	0.96 ± 36.16

XWT1 and WTC1: EXPxCS, XWT2 and WTC2: EXPxLS, WP1 = 4.8495 m; WP2 = 20.146 m; WP3 = 25.136 m; WP4 = 30.425 m; WP5 = 40.406 m; and WP6 = 50.609 m.

and 50.609 m are shown in Figures 2(b), (c) and (d), respectively. An excellent comparison between the numerical simulation based on CS and LS approaches with that of experimental measurements (EXP) can be seen from the above figures. The wave spectra for the surface elevation near the paddle (WP1) and far away from the paddle (WP6) are depicted in Figures 3(a) and (b). The wavelet power spectra for the experimental measurements at WP1 and WP6 are shown in Figures 3(c) and (d), respectively. The measured wave period is found to be close to 1.92 s. The COI where edge effects might have influence is shown as a white shade (the values within this region are presumably reduced in magnitude due to zero padding), the thick black contour designates the 95% confidence contours (energy concentration). In order to reveal the difference between the two time histories near to the paddle, the cross wavelet power and phase difference are shown in Figures 4(a) and (b) for EXP against CS and EXP against LS, respectively. The arrows indicate the relative phase difference between the two time series: the arrows pointing to the right indicate the in-phase, whereas the left arrows indicate out-of-phase. The arrows pointing downward indicate that the numerical simulation exhibits a phase shift of about 90° with respect to the experimental measurements. The figure shows that within the 95% energy concentration, the simulated time series is in phase with the experimental observation. The quantitative mean phase angle in the XWT for EXP-CS is $-2.28°\pm1.571°$ ($\pm$ indicates error estimated using the circular standard deviation), whereas for EXP-LS it is $-2.49°\pm1.470°$. The cross wavelet shows the existence of high common power between the two time series and, in order to reveal the phase lock behavior, the wave coherent transform is used. The squared wavelet coherent transform for EXP-CS and EXP-LS is shown in Figures 4(c) and (d), respectively. The area of the 95% confidence contour is large compared with the cross wavelet power, which shows the intensity of covariance irrespective of high common power. Significant wavelet coherence is found to exist for the wave period less than 1 s. In the region of primary frequency, the time series are in-phase as indicated by arrows and scattered elsewhere. The mean phase angle for squared WTC of EXP-CS and EXP-LS is $-1.82°\pm39.73°$ and $-1.36°\pm37.08°$, respectively. Similar kind of wavelet analysis has been carried out for all the time series measured at six different locations along the flume and only the quantitative results are depicted in Table I.

The numerical and experimental measurements for the wave height of 0.2 m along the various locations of the tank are shown in Figure 5. This simulation corresponds to a steepness of 0.047. When the distance from the wave paddle increases, the CS approach shows a slight phase shift even though the wave height is maintained constant. Qualitative wavelet analysis has been reported for the two time series for this case, one near to the paddle and the other far away from the paddle. The power spectra from fourier analysis for the wave surface elevation time histories at 4.895 m show the concentration of energy at 0.52 and 1.05 Hz, due to the existence of nonlinearity (Figure 6(a)).

DOI: 10.1002/fld

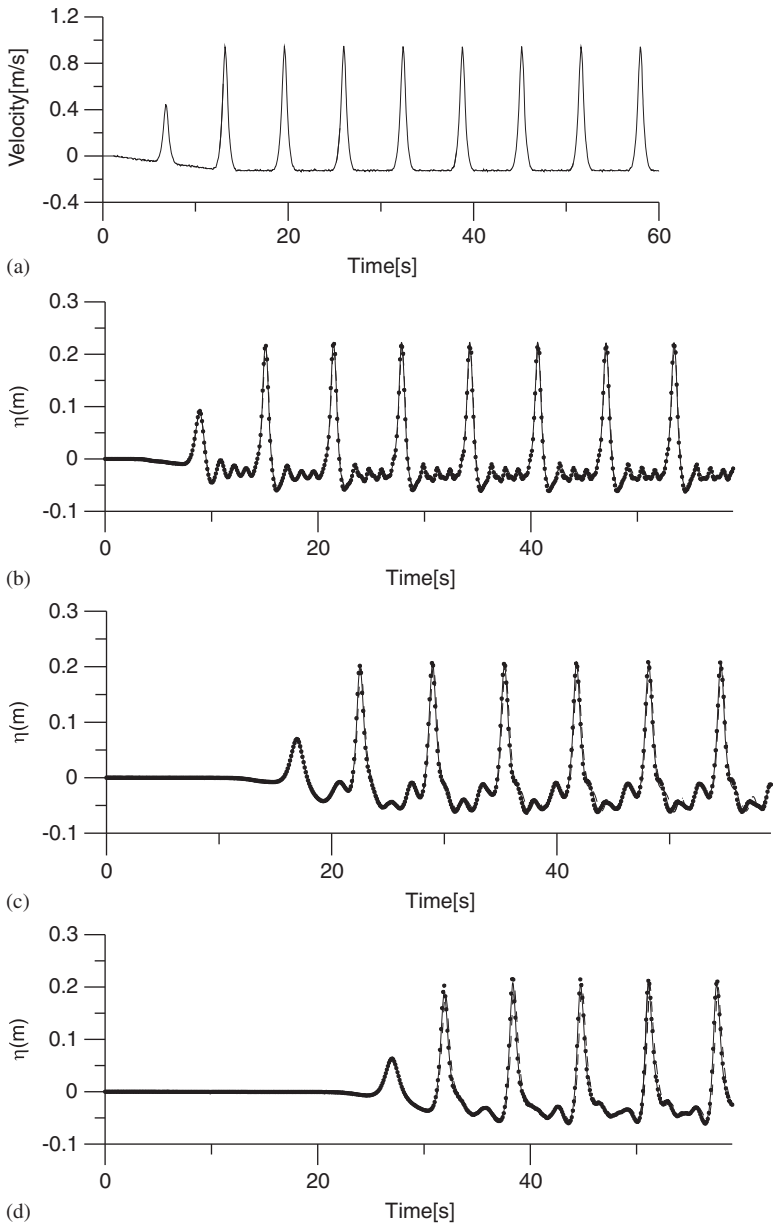

Figure 10. Cnoidal wave (CN2): (a) input velocity; (b) time history at 4.849 m; (c) time history at 25.136 m; and (d) time history at 50.609 m.

The wavelet power spectrum for the experimental measurement is also shown in Figure 6(b). The XWT for EXP-CS and EXP-LS is shown in Figures 6(c) and (d), respectively. For a medium steep wave, the time series of EXP-CS are in-phase at the primary period of 1.92 s, whereas, a positive phase difference at the secondary mode is observed. In the case of EXP-LS, the waves

DOI: 10.1002/fld

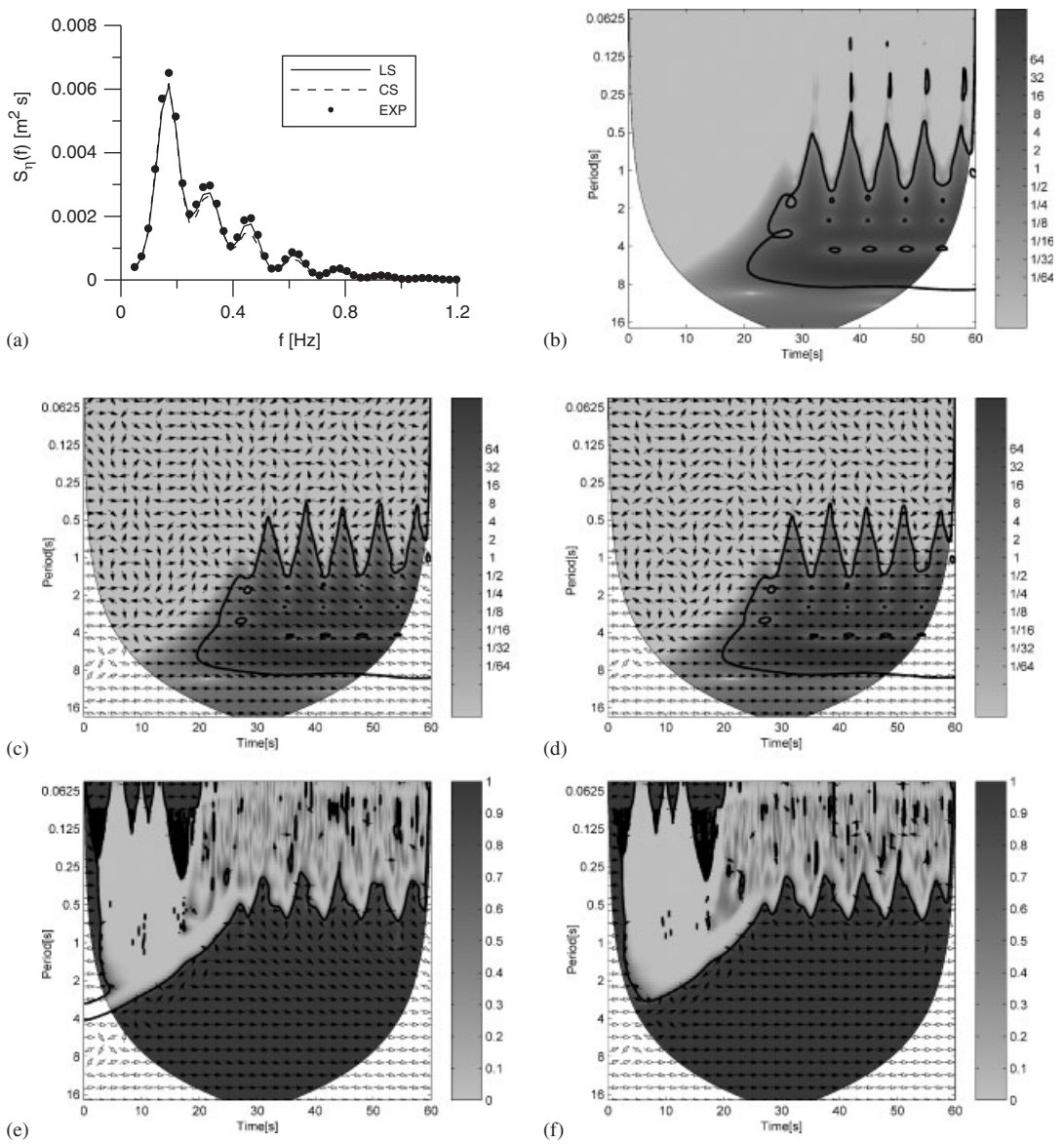

Figure 11. (a) Fourier spectrum at 50.609 m (CN2); (b) wavelet power for EXP at 50.609 m (CN2). Cross wavelet between (c) EXP-CS at 50.609 m (CN2) and (d) EXP-LS at 50.609 m (CN2). Wavelet coherence between (e) EXP-CS at 50.609 m (CN2) and (f) EXP-LS at 50.609 m (CN2).

are found to be in-phase within the 95% confidence contours. The squared WTC also reveals a similar behavior as shown in Figures 6(e) and (f). The XWT mean phase angle is $-4.95° \pm 15.24°$ and $-4.79° \pm 2.678°$ for EXP-CS and EXP-LS, respectively. A larger error for the CS approach has been noted compared with the LS approach. The power spectra from fourier analysis, CWT for experimental data, XWT and squared WTC for the time histories far away from the paddle are

DOI: 10.1002/fld

reported in Figure 7. The CS approach is found to advance compared to the measured wave surface elevation towards its direction of propagation. For the CS approach, this is noticed in the wavelet results both for primary as well as for secondary mode, whereas, such a difference is noticed only in secondary mode while adopting the LS approach. The quantitative results of this case for all the time series are presented in Table II. The phase shift is found to increase for CS approach compared to that for the LS approach. The reason for the CS method unable to capture the high-frequency waves is that a spline curve is fitted only on the free surface with 2 points on either side of the node under consideration. The x-coordinates and potential values at the respective locations are being used to evaluate the velocities, irrespective of the z values. Hence, when the waves become highly nonlinear, it is unable to capture the high-frequency oscillation, because of the smooth fitting of the CS approach. While, the LS method uses the underlying nodes also, i.e. the mesh nodes that connect the node under considerations, hence it is able to capture the high-frequency oscillations that encounters in the nonlinear waves. Thus, an algorithm that evaluates the velocity based on the nodes underlying the mesh will provide a better approximation when dealing with nonlinear wave simulation using FEM. Moreover, the phase angle is not a constant over the length of the tank which may be due to the uncertainty in the location of wave probes along the flume for the measurement of the wave time history. Probable reason for the small deviation in the lower period may be due to the fact that the input signal (paddle displacement) obtained from the paddle for the low period got polluted by the noisy signal when one differentiate to obtain the paddle velocity.

In order to know the wavelet phase angle error with respect to mesh size and time step, the mesh and time-independent studies are carried out for the steep regular waves. The number of nodes along the z-direction is kept constant and the number of nodes on the free surface is tested for three cases ($L/30$, $L/40$ and $L/50$, where L is wave length) with a constant time step of $T/100$ (wherein, T is wave period). The result for these test cases at WP3 and WP6 is shown in Table III(a) and (b), respectively. The table shows that as the mesh sizes increases the error tends to reduce and the optimum value is $L/40$. The numerical tests are then carried out for three different time steps ($T/60$, $T/100$ and $T/120$) with the constant mesh size ($L/40$). The results are shown in Table IV(a) and (b) for the wave gauge location at WP3 and WP6. The table shows that as the time step reduces the wavelet phase angle reduces and the optimum value is $T/100$.

5.2. *Cnoidal waves*

The nonlinearity in a shallow water wave is relatively more and is of practical relevance compared to the regular waves of higher-order propagating near the coast. Hence, an attempt has been made

Table VI. Wavelet phase angle for the test case $T=6.4$ s, $H=0.3$ m, $D=0.62$ m (CN2).

Wavelet	WP1 (deg.)	WP2 (deg.)	WP3 (deg.)	WP4 (deg.)	WP5 (deg.)	WP6 (deg.)
XWT1	6.4±5.62	12.11±21.84	13.70±17.50	19.43±17.30	19.86±19.04	19.72±17.91
WTC1	8.04±25.6	8.88±26.83	10.91±30.77	13.30±32.74	14.44±33.44	12.87±33.19
XWT2	1.59±3.37	2.16±11.68	2.14±9.26	3.59±7.56	2.95±4.72	0.57±4.08
WTC2	4.29±21.4	2.07±22.60	3.36±26.22	3.59±27.06	2.60±25.94	1.06±25.95

XWT1 and WTC1: EXPxCS, XWT2 and WTC2: EXPxLS, WP1 = 4.8495 m; WP2 = 20.146 m; WP3 = 25.136 m; WP4 = 30.425 m; WP5 = 40.406 m; and WP6 = 50.609 m.

DOI: 10.1002/fld

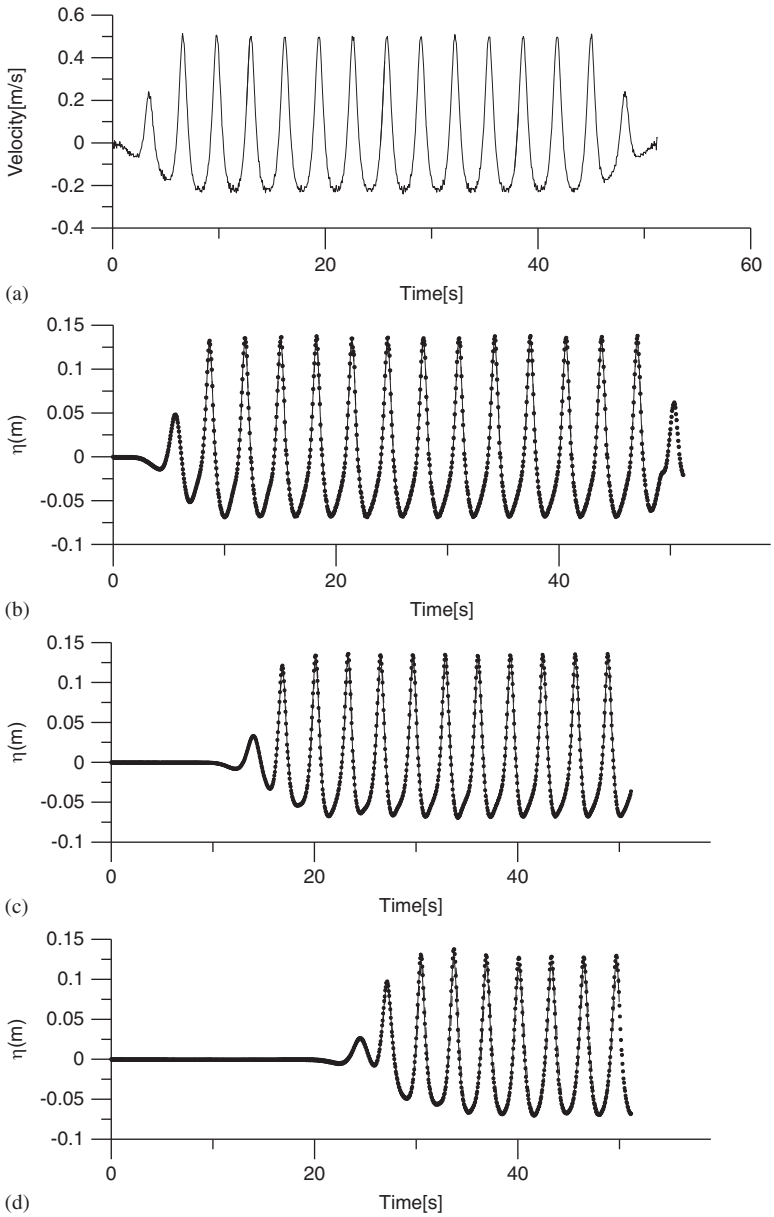

Figure 12. Cnoidal wave (CN3): (a) input velocity; (b) time history at 4.849 m; (c) time history at 25.136 m; and (d) time history at 50.609 m.

to understand the performance of the present numerical code for the simulation of shallow water waves such as cnoidal and solitary waves. In this section cnoidal waves of different characteristics were generated in the laboratory with Ursell parameter of 30, 307 and 41 that corresponds to CN1 ($H = 0.03\,\text{m}, T = 6.4\,\text{s}$), CN2 ($H = 0.3\,\text{m}, T = 6.4\,\text{s}$) and CN3 ($H = 0.2\,\text{m}, T = 3.2\text{s}$), respectively.

DOI: 10.1002/fld

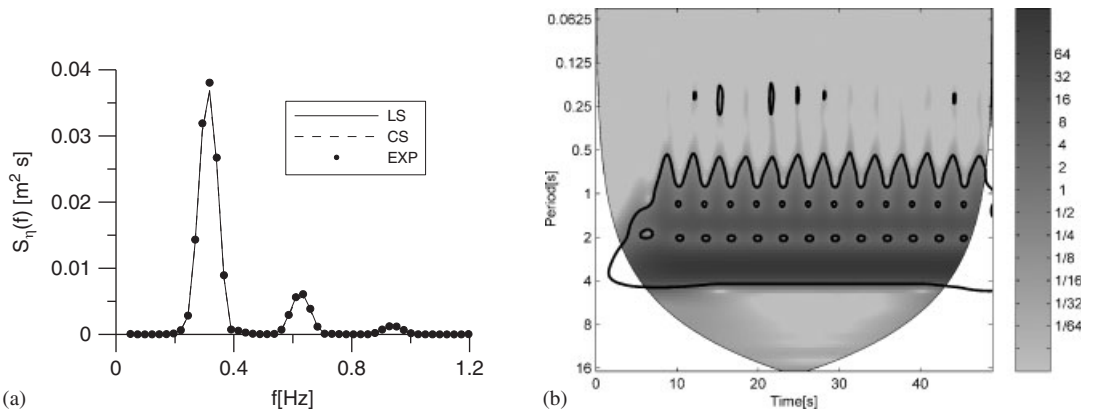

Figure 13. Fourier and wavelet spectrum for time history near to the paddle (CN3). (a) Fourier power spectra and (b) wavelet power for EXP.

Table VII. Wavelet phase angle for the test case $T=3.2$ s, $H=0.2$ m, $D=0.621$ m (CN3).

Wavelet	WP1 (deg.)	WP2 (deg.)	WP3 (deg.)	WP4 (deg.)	WP5 (deg.)	WP6 (deg.)
XWT1	3.19±4.42	11.67±7.87	12.00±6.52	15.95±9.9	20.43±12.30	16.39±9.32
WTC1	1.09±20.94	7.97±21.95	9.65±23.36	10.67±24.69	14.3±34.87	8.61±28.09
XWT2	0.12±3.14	1.49±2.85	0.76±1.57	5.71±4.68	2.60±3.12	−0.54±2.85
WTC2	0.21±20.35	0.43±18.84	0.79±20.93	3.68±21.50	1.93±29.66	−1.00±26.03

XWT1 and WTC1: EXPxCS, XWT2 and WTC2: EXPxLS, WP1 = 4.8495 m; WP2 = 20.146 m; WP3 = 25.136 m; WP4 = 30.425 m; WP5 = 40.406 m; and WP6 = 50.609 m.

The wave paddle signal is generated from the cnoidal wave theory and obviously the generated profile will not be stable during propagation due to the dispersion of many frequency components. A more stable cnoidal wave form could be achieved by using the formulation of Goring [27]. Since the main objective of this paper is to investigate the physical and numerical aspects of nonlinear wave simulation, a simple approach of wave generation using cnoidal wave theory is sought. The input wave paddle velocity and the generated wave elevation at a distance of 4.84 m, 25.136 m and 50.609 m from the wave paddle are depicted in Figure 8. The simulated wave profile using the approaches of CS and LS are superposed. An excellent agreement between both the numerical approaches with the measurements can be seen. The frequency spectrum of wave elevation at 50 m (Figure 9(a)) shows the peak period of 6.4 s. However, the spectrum is found to be broad. The corresponding wavelet power spectrum for the measurement (Figure 9(b)) shows that the 95% energy is concentrated within the wave period ranging between 1.5 to 1.8 s with a peak around 6.4 s. The phase angle estimated using XWT (Figures 9(c) and (d)) shows that in both the cases of CS and LS, the secondary mode (near 3 s) shows a positive phase shift, whereas the wave near the primary period is in-phase. The squared WTC is also shown in Figures 9(e) and (f) and the quantitative phase angle information inside the 95% energy levels is presented in Table V for all the simulated cnoidal profiles.

DOI: 10.1002/fld

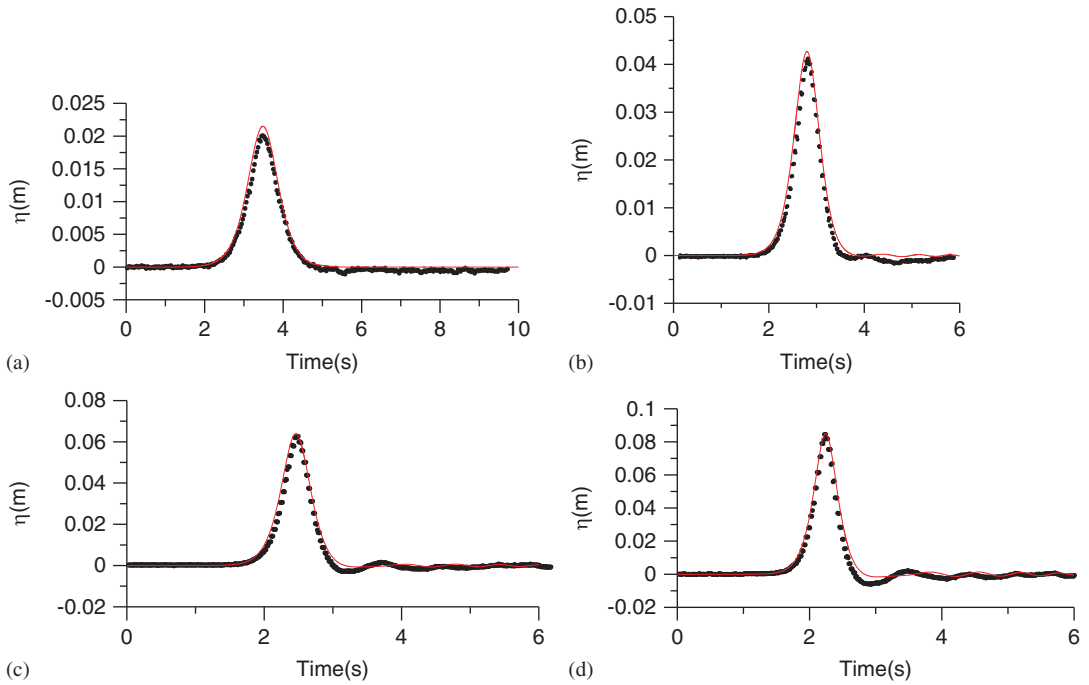

Figure 14. Comparison between numerical (line) and experiments (dotted). (a) $H/d=0.1$; (b) $H/d=0.2$; (c) $H/d=0.3$; and (d) $H/d=0.4$.

The measured time wave elevation history for CN2 and the numerical simulation at various distances from the paddle are shown in Figure 10. The comparison is found to be excellent. The measured and simulated frequency spectra for the wave elevation at 50.609 m are superposed in Figure 11(a). The experimental CWT (Figure 11(b)) shows a peak wave period of 6 s and the energy spreads over a period ranging from 0.5 to 8 s. The XWT shown in Figures 11(c) and (d) reveal that the simulation with CS approach exhibits a phase lag except near the primary period, while simulation using LS shows a lesser phase lag. However, the squared WTC (Figures 11(e) and (f)) shows a larger significant coherence for both the approaches of numerical simulation. The quantitative phase lag inside the 95% energy level is given in Table VI.

The measured wave elevation and its comparison with the simulation from the two numerical approaches for a wave period of 3.2 s (CN3) are shown in Figure 12. The fourier spectrum and CWT for the measured wave elevation near the paddle are shown in Figures 13(a) and (b). The energy concentration occurs over a period range of 0.5 s to 4 s, with a peak at 3.2 s. The analyses on XWT and WTC reveal similar observation as that for CN2. The mean phase angles in the 95% energy level for all the wave probes used in the laboratory investigation are reported in Table VII. For small wave steepness, the phase difference is found to be small, while for the medium wave steepness, the phase difference is very high for CS compared with that of LS approach.

5.3. Solitary wave

The generation of solitary waves has been carried out at University of Wuppertal, Germany. The generation of solitary waves by prescribing the piston-type wave maker motion is determined from

DOI: 10.1002/fld

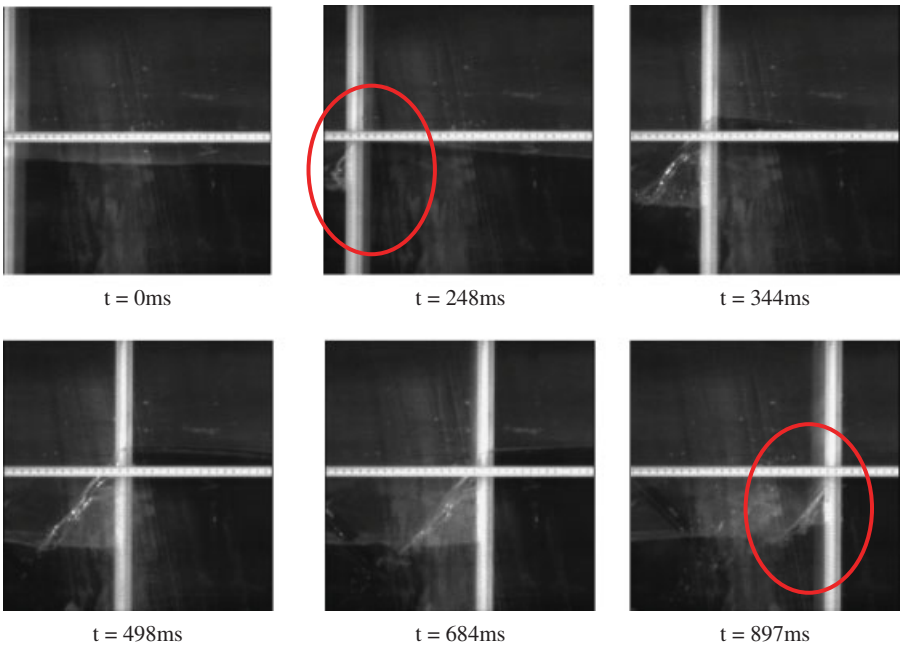

Figure 15. Snap shots of the water flowing through the side walls.

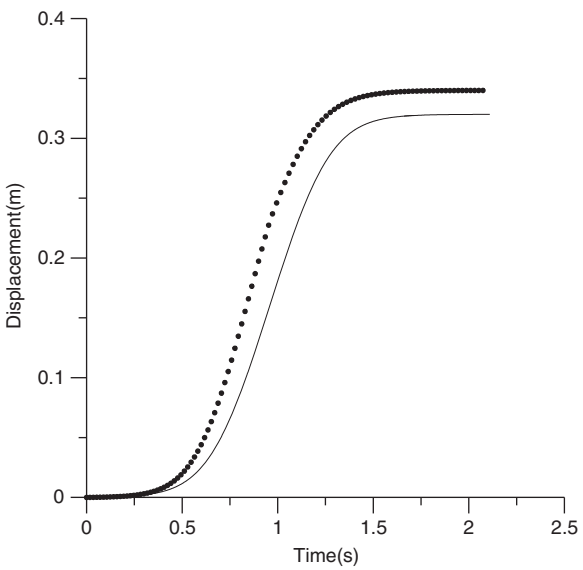

Figure 16. Generated signal (line) and the tuned signal (dotted) to the paddle to generate same wave height ($H/d = 0.1$).

DOI: 10.1002/fld

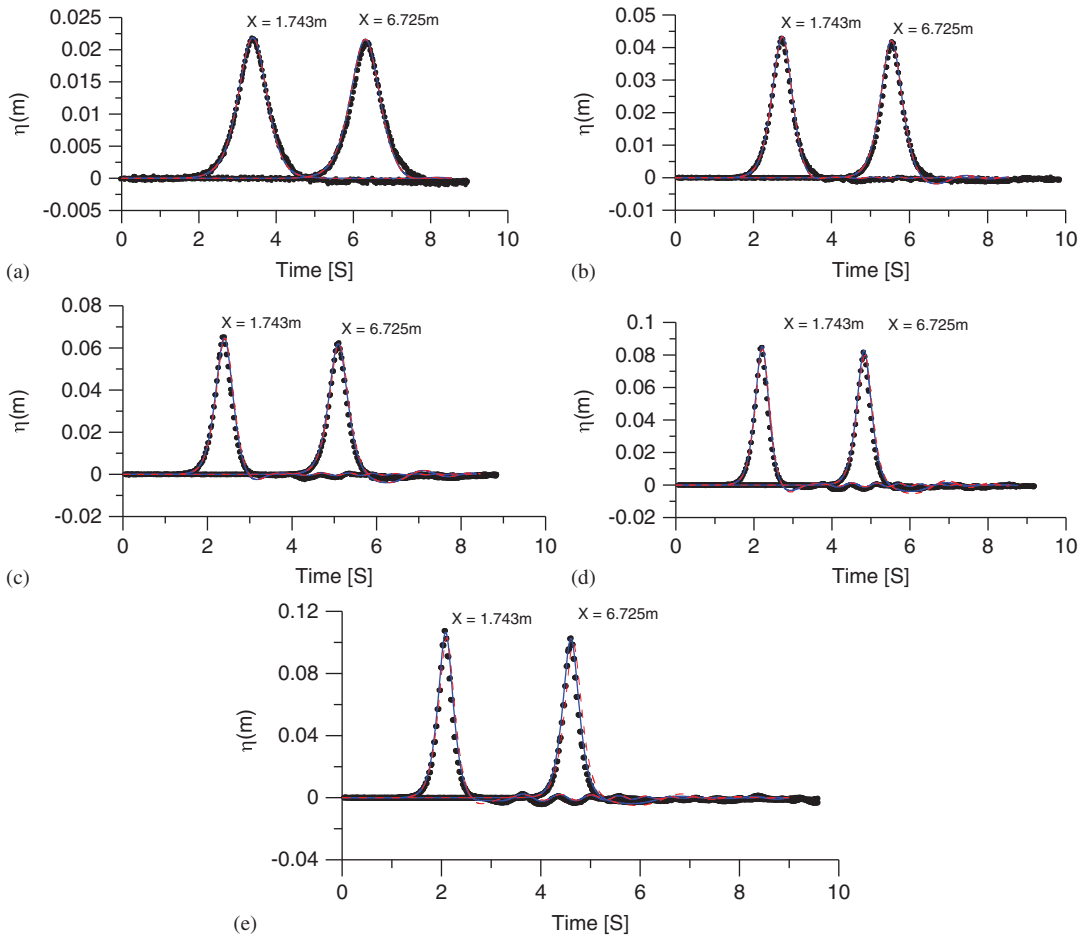

Figure 17. Comparison of time histories for experiments (dotted), least square (line), and cubic spline (dashed line). (a) $H/d=0.1$; (b) $H/d=0.2$; (c) $H/d=0.3$; (d) $H/d=0.4$; and (e) $H/d=0.5$.

the first-order Boussinesq wave theory [27]. The surface profile has been measured using ultrasonic probe at two locations. The experiments were carried out for $H/d=0.1$–0.5. Figures 14(a–d) present the comparison of measured wave elevation with the numerical simulation (based on LS). A slightly broader wave profile can be seen in the numerical simulation compared with the measured wave surface elevation for waves with smaller steepness. The simulation peak magnitude is also found to be higher. For steep waves, though the wave height remains the same, the width of the simulated solitons is wider. This is due to the difference in the displaced mass of the water even though the paddle signal is same. The loss of volume of water is accounted for the water flowing backward to the paddle through the gap between the wave paddle and the side walls when the paddle set into motion. As the width of the flume is small, this effect is more pronounced. The reason for the wave height remaining unchanged for the steeper waves is due to the fact that the paddle stroke is quite fast when compared with smaller steepness. This feature has been captured

DOI: 10.1002/fld

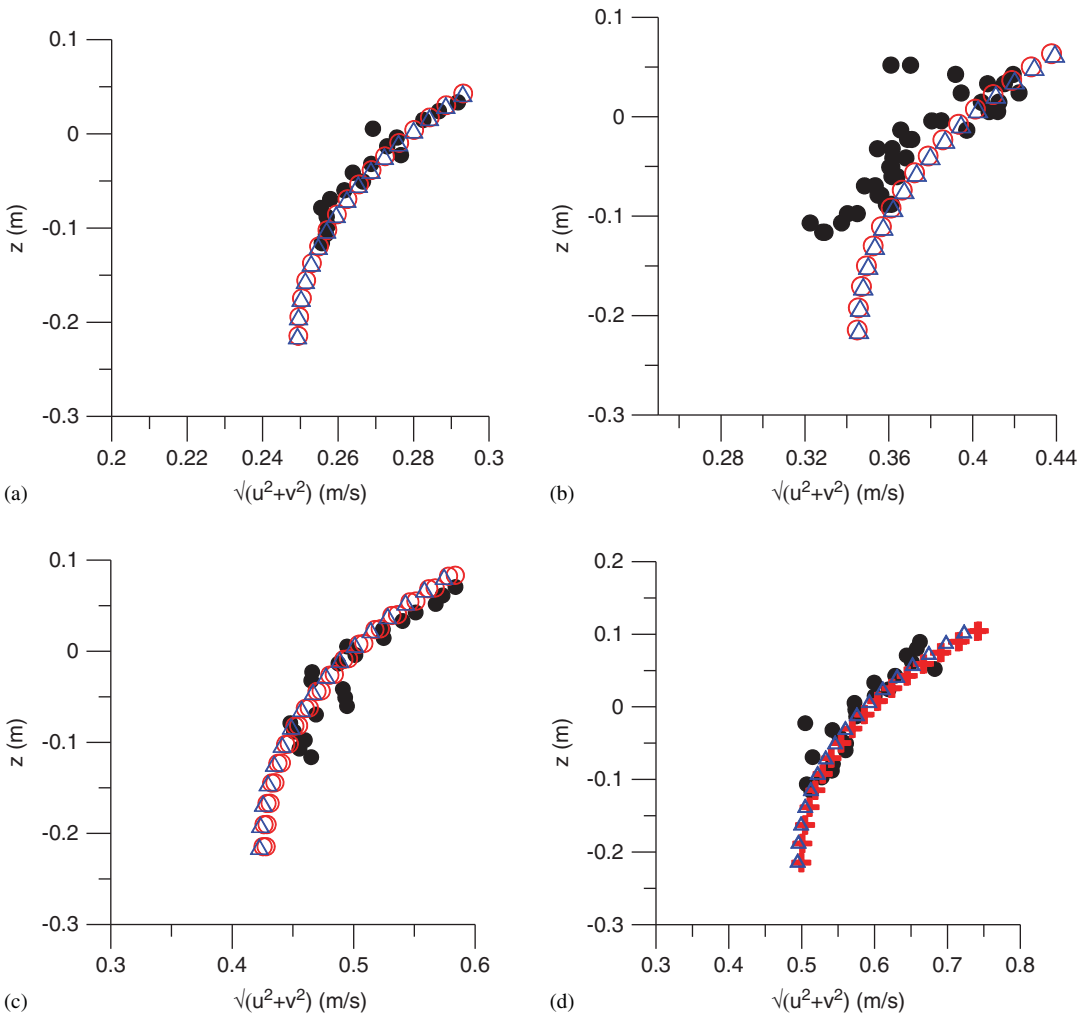

Figure 18. Velocity comparison between experiments (closed circle), LS (open circle) and cubic spline (triangle). (a) $H/h=0.2$; (b) $H/h=0.3$; (c) $H/h=0.4$; and (d) $H/h=0.5$.

using a high-speed camera and the various snap shots of the water flowing through the gaps are shown in Figure 15. One can minimize this effect by adjusting the input signal to generate the target wave height and profile using trial and error method. The input signal for the numerical model (i.e. the generated signal) and the signal given to the paddle (i.e. tuned signal) to generate a wave with specified characteristics are shown in Figure 16 for $H/d=0.1$. Since, the paddle displacements are different and the comparisons are made based on the wave profile alone, the wavelet analysis is not carried out. The comparison between the numerical simulation (CS and LS) and experimental measurements for waves with steepness ranging from 0.1 to 0.5 is shown in Figure 17. An interesting feature can be noted. After the soliton propagates, the oscillation is below the mean water surface (zero level), which once again proves that the water is flowing back through

DOI: 10.1002/fld

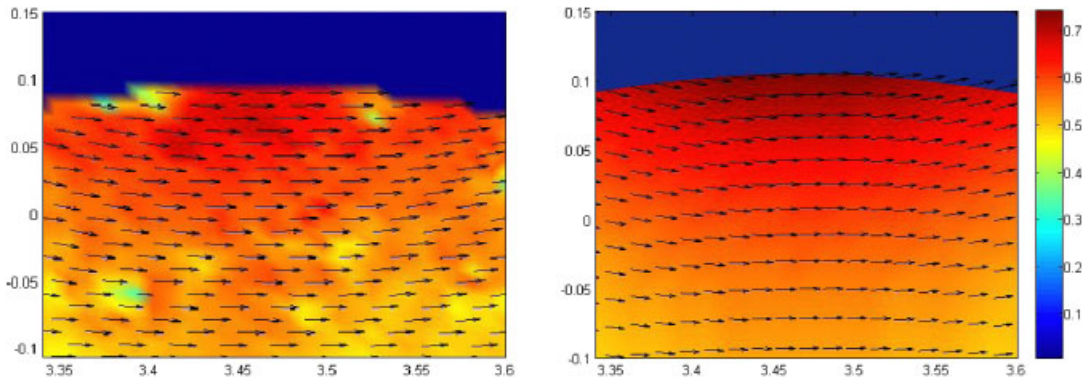

Figure 19. Spatial velocity information using experimental PIV measurement (left) and numerical simulation (right) for $H/d = 0.5$.

the side of the wave paddle after reaching the extreme position of the wave paddle. This eventually reduces the trailing waves that should be presented in solitary wave generation. But attempts are being made by several researchers for the minimization of trailing waves [28]. For higher wave steepness, the numerically simulated trailing waves are different from the measurement. CS shows a phase difference for steepness above 0.4. In order to reveal the water particle motion, due to which the phase difference exists, PIV measurements were carried out.

MATPIV developed by Sveen [29] has been used for the analysis. The comparison between the numerical simulation (LS and CS) and the experimental measurement for particle velocity at the crest is shown in Figure 18. The CS simulated particle velocity is taken at the crest irrespective of the phase difference. The figure shows a good comparison for velocity magnitudes using LS with that of EXP. The CS shows lower velocity magnitude for H/d greater than 0.4. The spatial velocity information using PIV and numerical simulation (LS) for $H/d = 0.5$ is depicted in Figure 19.

6. CONCLUSION

In this paper, the quantitative and qualitative analyses on the phase difference between the numerical wave simulation based on FEM and experimental measurements are reported. Two approaches for estimating the horizontal velocities based on CS and LS approaches have been explored in detail. The analysis has been carried out using the time–frequency analysis based on wavelets. The common high power has been shown using the cross wavelet transformation and phase lock behaviors are revealed using wavelet coherence. The analysis reveals that the waves simulated using CS lead the laboratory-generated steep waves. Even though the LS approach also leads the generated wave in the flume, the phase difference is found to be less compared with the former approach of simulation. The phase difference exists not at the primary period under investigation, but at the higher modes. Further, in our investigation the phase difference is not consistent along the length of the tank. The solitary wave measurements and the comparison with the numerical simulation are reported along with the crest particle velocity. CS and LS simulation behavior are same for small steep waves, whereas, the later approach shows promising for the medium to high steep waves. As the errors are minimal, both these approaches are quite acceptable and

DOI: 10.1002/fld

the numerical simulation can be successfully used as a replacement for physical modeling when simulation demands.

NOMENCLATURE

LS	least square approach
CS	cubic spline approach
EXP	experimental measurements
CWT	continuous wavelet transform
XWT	cross wavelet transform
WTC	wavelet coherence
FEM	finite element method
PIV	particle image velocimetry
MEL	mixed Eulerian and Lagrangian approach
COI	cone of influence
FOV	field of view

ACKNOWLEDGEMENTS

The experiments were carried out by the first author at the German Laboratories and the visit was supported by DAAD (German Academic Exchange Service) short term fellowship.

REFERENCES

1. Longuet-Higgins MS, Cokelet ED. The deformation of steep surface waves on water: I. A numerical method of computation. *Proceedings of the Royal Society of London, Series A* 1976; **350**:1–26.
2. Ma QW, Wu GX, Eatock Taylor R. Finite element simulation of fully nonlinear interaction between vertical cylinders and steep waves—part 1: methodology and numerical procedure. *International Journal for Numerical Methods in Fluids* 2001; **36**:265–285.
3. Westhuis JH. The numerical simulation of nonlinear waves in the hydrodynamic model test basin. *Ph.D. Thesis*, Universiteit Twente, The Netherlands, 2001.
4. Sriram V, Sannasiraj SA, Sundar V. Numerical simulation of 2D nonlinear waves using finite element with cubic spline approximations. *Journal of Fluids and Structures* 2006; **22**(5):663–681.
5. Wang CZ, Khoo BC. Finite element analysis of two-dimensional nonlinear sloshing problems in random excitation. *Ocean Engineering* 2005; **32**:107–133.
6. Sriram V, Sannasiraj SA, Sundar V. Velocity calculation methods in finite element based on MEL formulation. In *Advances in Numerical Simulation of Nonlinear Waves. Advances in Coastal and Ocean Engineering*, Ma QW (ed.), vol. 11. World Scientific Publishing Co.: Singapore, 2009.
7. Clauss GF, Steinhagen U. Numerical simulation of nonlinear transient waves and its validation by laboratory data. *Proceedings of the 9th International Offshore and Polar Engineering Conference*, Brest, France, 1999; 368–375.
8. Dommermuth DG, Yue DKP, Lin WM, Rapp RJ, Chan ES, Melville WK. Deep-water plunging breakers: a comparison between potential theory and experiments. *Journal of Fluid Mechanics* 1988; **189**:423–442.
9. Jensen A, Grue J. A note on the difference in the speed of gravity waves in a physical and numerical wave tank. *Wave Motion* 2002; **36**:41–48.
10. Schlurmann T. *Time Frequency Analysis Methods in Hydrology and Hydraulic Engineering*. Habilitationsschrift, Bergische Universität Wuppertal, Germany, 2004.
11. Balaji R, Sannasiraj SA, Sundar V. Detection of wave groups from the motion behavior of a discuss buoy. *Journal of Hydro-Environment Research* 2008; **1**(3–4):195–205.
12. Torrence C, Compo GP. A practical guide to wavelet analysis. *Bulletin of American Meteorological Society* 1998; **79**:61–78.

DOI: 10.1002/fld

13. Cointe R, Geyer P, King B, Molin B, Tramoni M. Nonlinear and linear motions of a rectangular barge in a perfect fluid. *Proceedings of the 18th Symposium on Naval Hydrodynamics*, Ann Arbor, MI, 1990; 85–99.
14. Wu GX, Eatock Taylor R. Finite element analysis of two dimensional non-linear transient water waves. *Applied Ocean Research* 1994; **16**:363–372.
15. Turnbull MS, Borthwick AGL, Eatock Taylor R. Wave–structure interaction using coupled structured–unstructured finite element meshes. *Applied Ocean Research* 2003; **25**:63–77.
16. Ma QW, Yan S. QALE-FEM for numerical modelling of nonlinear interaction between 3D moored floating bodies and steep waves. *International Journal for Numerical Methods in Engineering* 2008; DOI: 10.1002/nme.2505.
17. Sen D, Pawlowski JS, Lever J, Hinchey MJ. Two dimensional numerical modelling of large motions of floating bodies in waves. *Proceedings of the 5th International Conference on Numerical Modeling of Ship Hydrodynamics*, Hiroshima, 1989; 351–373.
18. Jain MK, Iyengar SRK, Jain RK. *Numerical Methods for Scientific and Engineering Computation*. New Age International Publishers: New Delhi, 2003.
19. Daubechies I. The wavelet transform time–frequency localization and signal analysis. *IEEE Transactions on Information Theory* 1990; **36**:961–1004.
20. Weng H, Lau KM. Wavelets, period doubling, and time–frequency localization with application to organization of convection over the tropical western Pacific. *Journal of the Atmospheric Sciences* 1994; **51**:2523–2541.
21. Meyers SD, Kelly BG, O'Brien JJ. An introduction to wavelet analysis in oceanography and meteorology: with application to the dispersion of Yanai waves. *Monthly Weather Reviews* 1993; **121**:2858–2866.
22. Liu PC. Wavelet spectrum analysis and ocean wind waves. In *Wavelets in Geophysics*, Foufoula-Georgiou E, Kumar P (eds). Academic Press: New York, 1994; 151–166.
23. Farge M. Wavelet transforms and their applications to turbulence. *Annual Review of Fluid Mechanics* 1992; **24**:395–457.
24. Zar JH. *Biostatistical Analysis*. Prentice-Hall: NJ, U.S.A., 1999.
25. Grinsted A, Moore JC, Jevrejeva S. Application of the cross wavelet transform and wavelet coherence to geophysical time series. *Nonlinear Processes in Geophysics* 2004; **11**:561–566.
26. Torrence C, Webster P. Interdecadal changes in the ESNO monsoon system. *Journal of Climate* 1999; **12**: 2679–2690.
27. Goring DG. Tsunamis—the propagation of long waves onto a shelf. *Ph.D. Thesis*, California Institute of Technology, Pasadena, CA, 1978.
28. Katell G, Eric B. Accuracy of solitary wave generation by a piston wave marker. *Journal of Hydraulic Research* 2002; **40**(3):321–331.
29. Sveen JK. *An Introduction to MatPIV V 1.6.1*, eprint series, Department of Mathematics, University of Oslo, Mechanics and Applied Mathematics. No. 2, 2004; ISSN: 0809-4403.